Journal of the Optical Society of America B
OPTICAL PHYSICS

Zero-crosstalk ultra-high-sensitivity dual-parameter sensor for magnetic field and temperature based on polarization-maintaining photonic crystal fiber

Weiqiang Wang,[1] Jingwei Lv,[1] Jianxin Wang,[1] Famei Wang,[2] Wei Liu,[1] Zao Yi,[3] Miao Liu,[4] Qiang Liu,[1] Paul K. Chu,[5,6,7] and Chao Liu[1,*]

[1]School of Physics and Electronic Engineering, Northeast Petroleum University, Daqing 163318, China
[2]Shenzhen Key Laboratory of Ultra-Intense Laser and Advanced Material Technology, Center for Intense Laser Application Technology, and College of Engineering Physics, Shenzhen Technology University, Shenzhen 518118, China
[3]Joint Laboratory for Extreme Conditions Matter Properties, Southwest University of Science and Technology, Mianyang 621010, China
[4]Qinhuangdao Campus, Northeast Petroleum University, Qinhuangdao 066044, China
[5]Department of Physics, City University of Hong Kong, Tat Chee Avenue, Kowloon, Hong Kong SAR, China
[6]Department of Materials Science and Engineering, City University of Hong Kong, Tat Chee Avenue, Kowloon, Hong Kong SAR, China
[7]Department of Biomedical Engineering, City University of Hong Kong, Tat Chee Avenue, Kowloon, Hong Kong SAR, China
*msm-liu@126.com

Received 4 June 2025; revised 13 July 2025; accepted 20 July 2025; posted 23 July 2025; published 15 August 2025

It is found that enhancing the loss peak can effectively suppress crosstalk during detection of the magnetic field (H) and temperature (T). Polarization-maintaining photonic crystal fiber (PM-PCF) exhibits excellent immunity to crosstalk coupling due to its high birefringence effect. By combining these two characteristics, a dual-parameter sensor for magnetic field and temperature based on PM-PCF is proposed. The sensor's prominent advantage lies in its breakthrough high-sensitivity characteristics and the first realization of zero-crosstalk sensing. By depositing a gold film on the inner walls of the air holes to excite the surface plasmon resonance phenomenon and filling magnetic fluid and polydimethylsiloxane as sensitive materials, the simultaneous detection of magnetic field and temperature is achieved. Numerical analysis demonstrates that within the ranges of 30–130 Oe for magnetic field and 26.5–30.5°C for temperature, the sensor exhibits a maximum magnetic field sensitivity of 67.35 nm/Oe and an average temperature sensitivity of 81.42 nm/°C. Compared with the current highest sensitivity, it still achieves a nearly twofold improvement. Additionally, this sensor has solved the crosstalk problem in dual-parameter sensors for temperature and magnetic field.

https://doi.org/10.1364/JOSAB.569869

1. INTRODUCTION

Magnetic field (H) and temperature (T) are key parameters in engineering applications, particularly in fields such as medical diagnostics, aerospace, and navigation [1–3]. Traditional magnetic field and temperature sensors are all based on electronic components. Magnetic field sensors include fluxgate, magnetotransistor, and magnetoresistor, while temperature sensors include thermocouple and thermistor [4–7]. They have practical disadvantages such as large volume, low sensitivity, slow response, and poor integration. In recent years, the development of optical fiber technology has promoted the application of surface plasmon resonance (SPR) in sensing. As early as 2007, Hassani and Skorobogatiy demonstrated the coupling mechanism of SPR-PCF [8], and various optical fiber sensors have been successively developed since then. Compared with electronic sensors, optical fiber sensors have advantages such as high sensitivity, small size, and fast response speed.

Driven by the trend toward integration, dual-parameter magnetic field and temperature optical fiber sensors have attracted significant attention. In 2017, Liu *et al*. first proposed a dual-parameter magnetic field and temperature sensor based on PCF [9]. The highest magnetic field sensitivity was 0.1927 nm/Oe, and the highest temperature sensitivity was 0.512 nm/°C. Subsequently, various dual-parameter magnetic field and temperature sensors emerged, mainly divided into two categories: longitudinal extension and transverse extension. Longitudinal extension realizes dual-parameter sensing by cascading magnetic field sensors and temperature sensors; transverse extension achieves dual-parameter sensing by integrating

two sensitive materials in the fiber cross section. Under these two branches, different improved schemes have been derived, mainly by changing the optical fiber type, sensitive materials, metal materials, and innovative structural design to enhance sensing performance.

Although cascaded dual-parameter sensors with longitudinal extension have simple manufacturing processes, their sensitivity is generally low. In 2024, Fu *et al*. designed a cascaded dual-parameter sensor for magnetic field and temperature by wrapping MF and PDMS on the surface of a gold-plated coreless optical fiber. Between 0 and 551 Oe, the maximum magnetic field sensitivity was 0.012267 nm/Oe, and between 30 and 70°C, the maximum temperature sensitivity was 1.662 nm/°C [10].

Due to flexibility, transverse extension demonstrates unique advantages in dual-parameter sensing. As early as 2020, Liu *et al*. proposed a dual-parameter magnetic field and temperature sensor that coated silver and graphene onto the central hole and filled the surrounding air holes with chloroform and toluene, which could achieve a maximum magnetic field sensitivity of 0.044 nm/Oe and a maximum temperature sensitivity of 0.37 nm/°C [11]. However, the surface of silver is extremely prone to generating an oxide film, and the magnetothermal properties of chloroform and toluene are not obvious, making the sensitivity of this sensor low. Therefore, in 2022, Wang *et al*. proposed another PCF-SPR dual-parameter magnetic field and temperature sensor coated with Ta_2O_5, using PDMS and MF as sensitive materials, with the highest magnetic field sensitivity and temperature sensitivity being 0.065 nm/Oe and 2.36 nm/°C, respectively [12]. With the improvement of manufacturing processes, Liu *et al*. designed a dual-parameter sensor based on anti-resonant optical fiber in 2024, whose magnetic field and temperature sensitivities were 0.3 nm/Oe and 10.8 nm/°C, respectively [13]. In the same year, Fu *et al*. proposed an ultra-high sensitivity dual-parameter magnetic field and temperature sensor with germanium-doped core dual-hole optical fiber, where the maximum magnetic field sensitivity could reach 6.4 nm/Oe, and the maximum temperature sensitivity was approximately 44.6 nm/°C [14]. The temperature sensitivity has made a qualitative leap, but its magnetic field sensitivity still has significant room for growth. Then in 2025, we proposed a sensor based on coreless optical fiber, with the maximum magnetic field sensitivity of 20.207 nm/Oe and the maximum temperature sensitivity of −8.423 nm/°C [15].

So far, the sensitivity of dual-parameter magnetic field and temperature sensors has been significantly improved. However, all these sensors have one problem: there is crosstalk between temperature and magnetic field. Crosstalk is mainly caused by the fact that changes in the refractive index (n) in one part of the fiber cross section will lead to changes in the distribution of n across the entire cross section. It is specifically manifested as: when one of T and H changes, all loss peaks will shift, making it impossible to accurately distinguish the influence degree of H and T. This is an inherent defect in optical fiber sensors. To solve the cross-sensitivity problem, all literatures use the method of matrix calculation to demodulate crosstalk, but this is only a rough calculation [16,17].

Through a large number of simulation calculations, it was found that the larger the peak value of the loss spectrum, the smaller the offset of the loss peak caused by crosstalk. When the peak value reaches a certain value, the offset of the magnetic field loss peak caused by temperature is 0 (with a precision of 0.001 nm level), that is, zero-crosstalk detection can be achieved. Based on the sensing principle of SPR optical fiber sensors, changes in a single physical quantity such as temperature or magnetic field will cause alterations in the overall refractive index distribution of the sensor, thereby leading to shifts in all loss peaks. By designing a specific optical field coupling structure, we have ensured that a change in one particular physical quantity only induces a shift in a single loss peak, thus achieving zero-crosstalk detection. The structure and size of the optical fiber sensor and the thickness of the gold film all play a decisive role in sensing loss. We designed a PM-PCF dual-parameter sensor by combining the anti-crosstalk characteristics of high loss peaks in optical fiber sensors with the high birefringence effect of polarization-maintaining fibers (PMFs) to simultaneously detect magnetic fields and temperature [18]. The sensor forms a rectangular core structure through two large elliptical holes. By means of the high refractive index difference between air and glass, the optical wave is confined to a very small core region, which greatly enhances the SPR coupling effect. By adjusting the structural parameters of the PM-PCF dual-parameter sensor until the loss spectrum exhibits a high loss peak state, zero-crosstalk dual-parameter detection based on the loss spectrum is realized. Only the offsets of the two loss peaks need to be calculated respectively to accurately detect the magnetic field and temperature. At the same time, five air holes are set in the core to adjust the SPR coupling process to achieve higher sensitivity. The modal characteristics of the sensor were analyzed using COMSOL. Important structural parameters, such as the core air hole diameter, the short semi-axis of the elliptical air hole, gold film thickness, and cladding air hole diameter, were optimized. Numerical analysis shows that when the magnetic field and temperature are in the ranges of 30–130 Oe and 26.5–30.5°C, respectively, the maximum magnetic field sensitivity can reach 67.35 nm/Oe, and the average temperature sensitivity can reach 81.42 nm/°C [14,15]. At the same time, the sensor eliminates the crosstalk problem during simultaneous detection of temperature and magnetic field, achieving high-precision detection.

2. MODEL AND THEORY

Figures 1(a)–1(c) show the design process of the sensor. Due to the high birefringence effect, the PMF enables the sensor to have different n for two orthogonal polarization modes (fast axis and slow axis), and the polarization state of light is confined to propagate along these axes, thereby avoiding random coupling of polarization states. When detecting magnetic fields, this characteristic helps reduce disturbances caused by temperature changes. PMFs are mainly divided into: PANDA PMF [19,20], which generate an asymmetric stress field through circular stress rods on both sides of the core; and Bow-Tie PMF, which adopt a trapezoidal stress zone design and core-type fiber to achieve birefringence through geometric asymmetry [21,22]. The core-type fiber has a flexible structure and is easier to obtain a high birefringence coefficient than PANDA and Bow-Tie polarization-maintaining fibers. As previously mentioned,

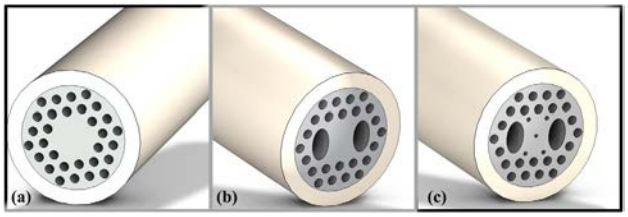

Fig. 1. Design process of a zero-crosstalk ultra-high sensitivity dual-parameter sensor for magnetic field and temperature based on PM-PCF.

increasing the peak value of the core light wave loss spectrum can improve the sensor's anti-interference capability, and the increase in the loss spectrum peak is caused by an increase in the real part of the effective refractive index (n_{eff}) of the core light wave. When the n of the optical fiber-sensitive material filling area changes, the n_{eff} of the light wave is relatively large, so the change in the overall refractive index distribution of the fiber cross section has almost no effect on it. At a precision level of 0.001 nm, the offset of the loss peak caused by crosstalk is zero, achieving zero-crosstalk detection. To increase the loss peak is to weaken the intensity of the core optical wave signal, and the most effective method is to form a polarization-maintaining core structure by setting two elliptical holes in the core region. The light guiding system under this structure ensures that the polarized light wave undergoes a strong SPR effect with the metal material, and most of the energy is coupled from the core area to the metal area, leading to a significant increase in the loss peak. Based on the above waveguide principles, we designed a PM-PCF sensor with a rectangular core structure and a high loss peak.

Figure 2(a) shows a traditional index guiding-photonic crystal fiber (IG-PCF) with an equilateral triangular lattice, and its fiber cross section exhibits C_{6v} symmetry (a structure with C_{nv} symmetry means that the structure coincides with the original structure after rotating any multiple of $360°/n$ around its center and has n different symmetry lines). The C_{nv} symmetry ensures the degeneracy of the two fundamental modes in the PCF. The PCF shown in Fig. 1(b) modifies two symmetrical holes adjacent to the core into elliptical shapes on the basis of an IG-PCF, reducing the fiber symmetry from the original C_{6v} to C_{2v}, so that the two fundamental modes of the fiber are no longer degenerate. The principle of birefringence can be achieved by forming a rectangular core structure in the y-direction. Light is confined in the core area by two elliptical holes, and the light field can be confined to a very small area by virtue of the high refractive index difference between air and glass. This gives it excellent confinement, greatly improves the SPR coupling degree, increases the SPR loss peak value, and thus suppresses the detection crosstalk between temperature and magnetic field. As shown in Fig. 1(c), symmetrically arranged small circular air holes are simultaneously set in the core to fine-tune the SPR coupling process to achieve higher sensitivity.

As shown in Fig. 2(a), the sensor can be fabricated through the following processes. First, femtosecond laser technology is used to drill holes in a quartz rod based on predesigned structural parameters to create a preform [23–25]. Subsequently, the preform is drawn into shape using a fiber drawing machine.

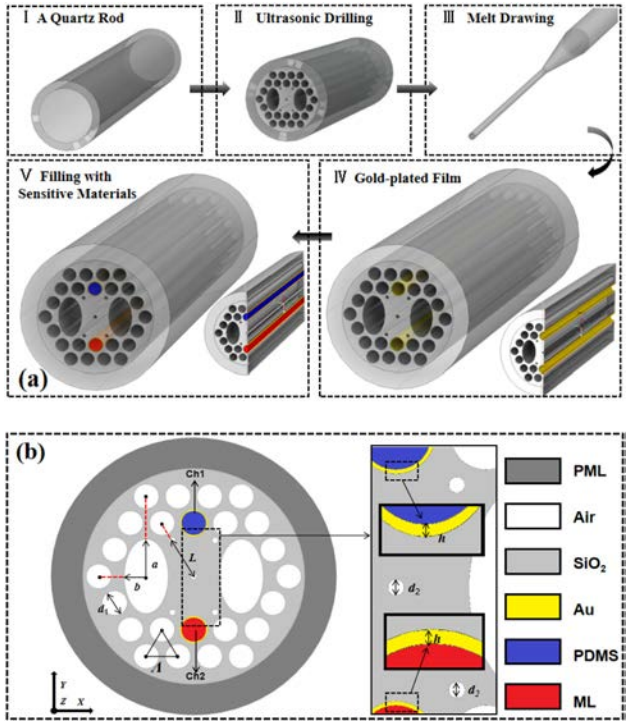

Fig. 2. (a) Manufacturing process of the SPR-PCF sensor and (b) cross-sectional structure of the SPR-PCF sensor.

Liquid phase deposition is then carried out to coat a gold film inside the holes [26]. Finally, PDMS (with a mixing ratio of 10:1 between the PDMS polymer and the curing agent) and MF are filled into Channel 1 (Ch1) and Channel 2 (Ch2), respectively, which have been coated with gold films [27–29]. The cross-sectional structure of the sensor is illustrated in Fig. 1(b), where the diameter of the cladding air holes is denoted as d_1, the pitch as Λ, the diameter of the core air holes as d_2, the pitch as L, the minor axis of the elliptical air holes as a, the major axis as b and the thickness of the gold film as h. The diameter of the optical fiber cladding is fixed at 80 μm.

Within a small temperature range, the Drude–Lorentz model describes the dielectric constant of gold [30]:

$$\varepsilon_{\text{Au}}(\omega) = \varepsilon_1 + i\varepsilon_2 = \varepsilon_\infty - \frac{\omega_p^2}{\omega(\omega + i\omega_c)}, \tag{1}$$

where ε_1 and ε_2 are the real and imaginary parts of the dielectric constant, respectively, $\varepsilon_\infty = 9.48$ is the dielectric constant of gold at high frequencies, ω is the angular frequency of the incident light, $\omega_p = 1.36 \times 10^{16}$ rad/s represents the angular frequency of the plasma, and $\omega_c = 1.45 \times 10^{14}$ rad/s represents the damping frequency. The refractive index of air is 1. The sensor is made of fused silica (SiO_2). Since this sensor measures temperature, it is necessary to use Sellmeier equation with a temperature parameter [15]:

$$n^2(\lambda, T) = 1.31552 + A_1 T + \frac{(B_1 + B_2 T)\lambda^2}{\lambda^2 - (B_3 + B_4 T)} + \frac{(C_1 + C_2 T)\lambda^2}{\lambda^2 - 100}, \tag{2}$$

where n is the refractive index of SiO_2, λ is the wavelength of the incident light, T is the ambient temperature, $A_1 = 6.90754 \times 10^{-6}$, $B_1 = 0.788404$, $B_2 = 2.35835 \times 10^{-5}$, $B_3 = 0.0110199$, $B_4 = 0.584758 \times 10^{-6}$, $C_1 = 0.91316$, and $C_2 = 0.548368 \times 10^{-6}$.

PDMS is a polymer with strong adhesion strength and a large thermo-optic coefficient. Compared to volatile ethanol, PDMS has better mechanical properties, processability, and stability. Its refractive index is calculated by the following formula [31]:

$$n_{\mathrm{PDMS}} = -4.5 \times 10^{-4} T + 1.4176. \tag{3}$$

Changes in the magnetic field and temperature cause the movement of magnetic nanoparticles in the MF and alter the optical properties of the MF. The refractive index of MF is represented by the Langevin model [32]:

$$n_{\mathrm{MF}} = (n_s - n_0)\left[\coth\left(\alpha\frac{H - H_{c,n}}{T}\right) - \frac{T}{\alpha(H - H_{c,n})}\right] + n_0, \tag{4}$$

where $n_s = 1.4385$ represents the saturated refractive index of MF, $n_0 = 1.4352$ is the initial refractive index of MF, $\alpha = 5$ is the fitting coefficient, $H_{c,n} = 30$ Oe is the magnetic field threshold, and H is the intensity of the environmental magnetic field.

When the core mode of the fiber and the surface plasmon polariton (SPP) mode satisfy phase matching at a certain wavelength λ, their n_{eff} are equal, and resonance occurs. A significant amount of the energy from the core mode is coupled to the SPP mode, thereby increasing the loss of the core mode. At this point, the loss spectrum of the core mode reaches an extremum. Changes in the magnetic field and temperature alter the n of the sensing materials and the phase-matching condition, causing a shift in the loss spectrum. Therefore, the sensing characteristics can be determined by the loss spectrum of the core mode [14]:

$$\alpha_{\mathrm{loss}} = 8.686\frac{2\pi}{\lambda}\,\mathrm{Im}(n_{\mathrm{eff}})10^7\left(\frac{\mathrm{dB}}{\mathrm{cm}}\right), \tag{5}$$

where λ is the wavelength of the incident light, and $\mathrm{Im}(n_{\mathrm{eff}})$ is the imaginary part of the effective refractive index.

When the core mode resonantly couples with the SPP mode, the loss spectrum of the core mode reaches an extremum. The wavelength at this point is called the resonance wavelength (RW). When the ambient temperature or magnetic field changes, the phase-matching condition changes, causing a shift in RW. Therefore, H and T can be monitored by determining the changes in RW This PM-PCF dual-parameter magnetic field and temperature sensor has no crosstalk issue, so the shift of the resonance peak can be directly used to accurately calculate the magnetic field and temperature sensitivities:

$$S_T = \frac{\Delta\lambda_{\mathrm{peak1}}}{\Delta T}, \tag{6}$$

$$S_H = \frac{\Delta\lambda_{\mathrm{peak2}}}{\Delta H}, \tag{7}$$

where S_T and S_T are the temperature sensitivity and magnetic field sensitivity, respectively, $\Delta\lambda_{\mathrm{peak1}}$ and $\Delta\lambda_{\mathrm{peak2}}$ are the wavelength shifts corresponding to peak point1 and peak point2 of the loss spectrum. ΔT is the change in temperature, and ΔH is the change in the magnetic field [15].

3. MODAL CHARACTERISTICS

When total reflection of light occurs in the core, the evanescent wave penetrating the metal film impacts the free electrons inside to form surface plasmon polaritons (SPPs). When the SPP wave and the core wave of a specific wavelength satisfy the phase matching condition, a resonant coupling phenomenon occurs, leading to the formation of a loss peak in the loss spectrum, and the position of the loss peak is affected by the n near the metal film [33]. In fact, the n of MF and PDMS will change with the variation of H and T [34]. Therefore, by filling the sensitive material into the gold-plated air holes, H and T can be indirectly detected by analyzing the changes in the loss peak.

The structure of the model does not possess rotational symmetry, resulting in different n_{eff} for the x-polarized (x-pol) core mode and the y-polarized (y-pol) core mode and different electromagnetic characteristics. This is exactly the characteristic of PMF. From the perspective of the interaction between light and matter, the importance of the electric field and magnetic field in a light wave is not the same. The effect of the magnetic field of a light wave on charged particles is much weaker than that of the electric field, so we only analyze the electric field [14]. Figure 3(a) depicts the loss spectra of the x-pol core mode and y-pol core mode at T of 25°C and H of 35 Oe. It can be observed that the loss spectrum of the y-pol core mode has a more pronounced loss peak. This can be explained by the electric field diagram in Fig. 3(b). The electric field direction of the y-pol core mode is orthogonal to the plane of the gold film, while the electric field direction of the x-pol core mode is parallel to the gold film. This causes the energy of the y-pol core mode to more easily couple with the gold film, consequently forming a sharp loss peak. Sharp loss peaks enable precise quantification of SPR coupling effects.

Figure 3(a) also shows that the PM-PCF of this structure has a high birefringence effective time difference, which can

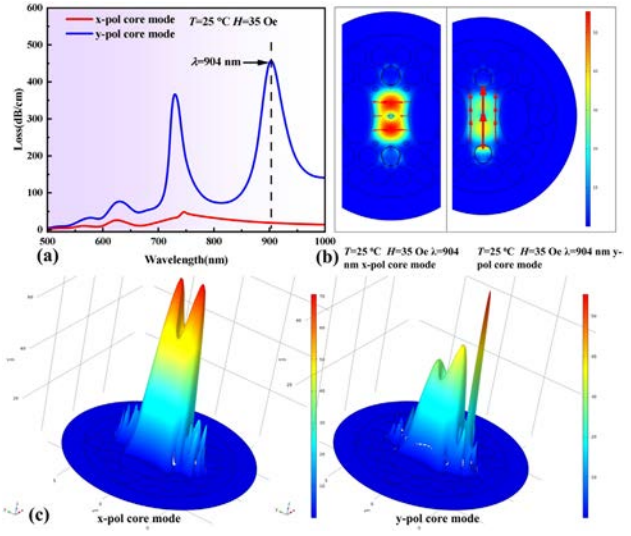

Fig. 3. (a) Loss spectra of the x-pol core mode and y-pol core mode and electric field distributions of the x-pol core mode and y-pol core mode; (b) 3D mode field distribution models of x-pol and y-pol.

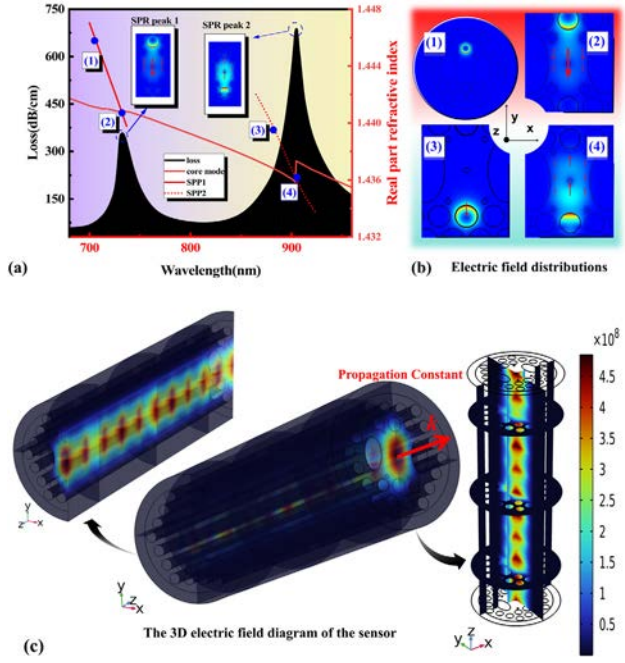

Fig. 4. (a) Effective refractive indexes of the y-pol core mode and SPP modes and loss spectrum of the SPR-PCF sensor; (b) electric field distributions of first-order SPP mode; and (c) the 3D electric field diagram of sensor.

effectively suppress the coupling crosstalk problem between modes. Therefore, the y-pol core mode is chosen in our subsequent analysis. Figure 3(c) shows the 3D electric fields of the x-pol core mode and y-pol core mode when $\lambda = 904$ nm, further illustrating that most of the energy of the y-pol core mode is coupled near the gold film, while the energy of the x-pol core mode is mainly distributed inside the core. Therefore, through the analysis of the y-pol core mode, this sensor can be used to detect magnetic fields and temperature.

By studying the loss spectrum of the y-pol core mode, the magnetic field and temperature can be determined. For an ambient temperature of 29°C and magnetic field strength of 38 Oe, the variation of the real part of the effective refractive index ($\mathrm{Re}(n_{\mathrm{eff}})$) for the y-pol core mode and the first-order SPP mode with wavelength, as well as the loss spectrum of the y-pol core mode, are shown in Fig. 4(a). There are two loss peaks in the loss spectrum, with SPR peak 1 at 733 nm and SPR peak 2 at 905 nm. Since Ch1 is filled with PDMS and Ch2 with MF, Ch1 is sensitive to temperature and Ch2 to magnetic fields. In the inset electric field diagram in Fig. 4(a), the intersections at points (2) and (4) of the three lines are precisely at the extreme points of the loss peaks; at this time, the $\mathrm{Re}(n_{\mathrm{eff}})$ of the SPP mode and y-pol core mode is equal, thus conforming to the phase-matching condition of SPR. At this point, the resonance condition is satisfied, and the loss is maximum [12].

Among all the optical wave modes transmitted within the fiber core, the core mode has the shortest cut-off wavelength and the highest corresponding cut-off frequency. When filtering and modulating the optical signal later on, if higher-order modes are analyzed, lower-order modes will definitely exist, which leads to a chaotic optical signal and makes it difficult to find the characteristic values of the optical signal. By setting the cut-off wavelength to the value corresponding to the core mode, only the core mode exists within the sensor, which aids in subsequent signal analysis. Additionally, based on COMSOL, the electric field distribution of the first-order SPP mode is shown in Fig. 4(b), with (1) to (4) showing the electric field patterns corresponding to the SPP modes at the four marked points in Fig. 4(a). At the wavelengths corresponding to SPR peak 1 and SPR peak 2, the electric field distribution of the SPP mode is more toward the core, thus verifying that SPR is excited at this wavelength.

Moreover, the electric field variation within the fiber cross-section is exactly half of a period. This half-period electric field variation image is both simple and can satisfy the requirements for SPR. Therefore, we only analyze the core mode and the first-order SPP mode. Figure 4(c) is a 3D electric field diagram of the sensor, further illustrating the sensing path of the light wave within the fiber core.

When H and T change, the loss peak of the y-pol core mode shifts, as shown in Fig. 5. Figure 5(a) reveals that when T is constant, the SPR peak 2 exhibits a redshift with increasing H, while the SPR peak 1 remains fixed. Therefore, the SPR peak 2 can be utilized for H detection, with an average sensitivity of 27.5 nm/Oe, whereas that of the SPR peak 1 is determined to be 0 nm/Oe. As shown in Fig. 5(b), when H is constant, the SPR peak 1 blueshifts with increasing T, while the SPR peak 2 remains unchanged. Consequently, the SPR peak 1 enables T detection with an average sensitivity of 30 nm/°C, whereas the SPR peak 2 shows 0 nm/°C. This sensor achieves ultra-high sensitivity and zero crosstalk for both H and T. Next, the structural parameters will be optimized to further enhance the sensing performance.

4. STRUCTURAL PARAMETER OPTIMIZATION

Since sensitivity is the most important performance indicator, the magnetic field sensitivity (S_H) and temperature sensitivity (S_T) are used as the main optimization criteria. In addition, the total sharpness (S_{SUM}) of the two resonance peaks and the spacing (W_{SEP}) between the two resonance peaks are also important bases for parameter optimization. $S_{\mathrm{SUM}} = \mathrm{Sh}_1 + \mathrm{Sh}_2$, where Sh_1 and Sh_2 are the sharpness values of SPR peak 1 and SPR peak 2, respectively. The spacing between the two resonance peaks (W_{SEP}), $W_{\mathrm{SEP}} = W_1 - W_2$, where W_1 and W_2 are the wavelength values corresponding to SPR peak 1 and SPR peak 2, respectively. The larger the S_H and S_T, the higher the sensitivity; the larger the W_{SEP}, the higher the distinguishability of the SPR peaks and the larger the detection range; the greater the sharpness, the higher the detection accuracy of the sensor. The performance of this sensor depends on the coupling between the y-pol core mode and the SPP mode, and the coupling between them is determined by the refractive index distribution near the gold film. The characteristic of photonic crystal fiber is that the refractive index distribution of the fiber cross section can be adjusted by changing the structural parameters of the air holes. We optimize according to the manufacturing process sequence of the sensor. First, holes are drilled from the center of the glass rod outward, and then a gold film is plated in the cladding air holes. Therefore, the optimization sequence of the structural parameters is: core air hole diameter d_2, elliptical air

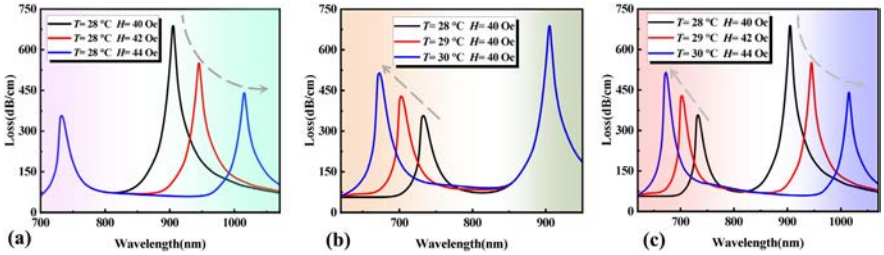

Fig. 5. (a) Loss spectra of the sensor as a function of H under a fixed temperature $T = 28°C$; (b) the loss spectra of the sensor as a function of T under a fixed magnetic field $H = 40$ Oe; and (c) the loss spectra of the sensor when both T and H vary simultaneously.

hole short semi-axis b (elliptical long semi-axis $a = \sqrt{3} \times b$), cladding air hole diameter d_1, and gold film thickness h, while other structural parameters are fixed: center air hole spacing $L = 17$ μm and cladding air hole spacing $\Lambda = 8.5$ μm. Various structural parameters interact to form a systematic and interactive closed loop [15].

A. Core Air Hole

First, the diameter of the core air hole is optimized, as shown in Figs. 6(a)–6(d). The value of d_2 ranges from a minimum of 0 μm up to 3.2 μm. If d_2 is further increased, the spacing between the air holes will become excessively narrow, making the air holes highly susceptible to deformation or even rupture during the fiber drawing process. Figure 6(a) presents the three-dimensional models of the sensor with different d_2 values (0, 0.8, 1.6, 2.4, and 3.2 μm) while keeping other parameters fixed ($d_1 = 5$ μm, $d_2 = 1.6$ μm, $L = 17$ μm, $b = 4.5$ μm, $a = \sqrt{3} \times b$, $h = 40$ nm). The loss spectra of the sensor's y-pol core mode are shown in Fig. 6(b). Under the environmental conditions of $T = 29.5°C$ and $H = 37$ Oe, the loss spectra exhibit a redshift phenomenon as d_2 increases. This is because the increase in d_2 reduces the n_{eff} of the y-pol core mode. According to the formulas $n = c/v$ (where c and v are the speeds of light in a vacuum and the medium, respectively) and $\lambda = v/f$ (where f is the intrinsic frequency of light), since the frequency of light remains constant in different media, the wavelength λ increases, and this increase causes the redshift. Figure 6(c) compares the loss spectra of the sensor under three different temperature and magnetic field conditions ($T = 29.5°C$, $H = 37$ Oe; $T = 30.5°C$, $H = 38$; and $T = 31.5°C$, $H = 39$ Oe) with varying d_2 values. Figure 6(d) summarizes the sensor's performance characteristics. As shown, when $d_2 = 1.6$ μm, the S_H of the sensor reaches a maximum value of 30.024 nm/Oe. When $d_2 = 2.4$ μm, the S_T and S_{SUM} reach their peak values, which are 35°C/nm and 52.55 dB/μm^2, respectively. Additionally, the W_{SEP} exhibits a slowly increasing trend with the increase of d_2 but shows no significant changes. Considering all performance indicators, $d_2 = 2.4$ μm is ultimately selected.

B. Semi-Minor Axis of Elliptical Air Hole

Next, we optimize the minor semi-axis b of the elliptical air holes, and the results are shown in Figs. 7(a)–7(d). The optimization range of b is from 3.5 μm to 7.5 μm. This is because when $b < 3.5$ μm, the core shape of the sensor begins to become square, and the polarization-maintaining property of the

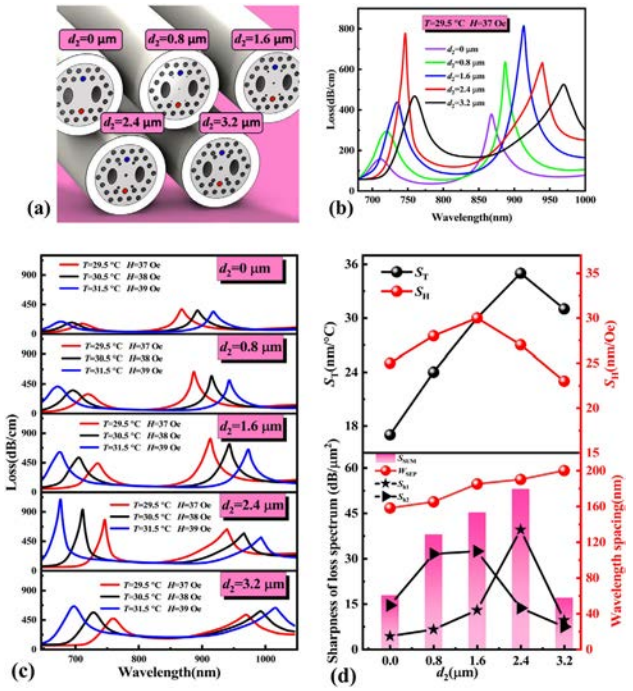

Fig. 6. When d_2 varies from 0 to 3.2 μm, (a) 3D models of the sensor, (b) changes in the loss spectrum under fixed T and H conditions, (c) comparison of the sensor's loss spectra under different T and H conditions, and (d) summary and comparison of the sensor performance as a function of d_2.

sensor starts to be lost. At this point, the confinement of the air holes to the y-pol core mode no longer has an advantage, and the coupling between the y-pol core mode and the SPP mode is significantly weakened. When $b > 7.5$ μm, as previously described, the gaps between the air holes are too narrow, making fabrication difficult and the structure prone to damage. Figure 7(a) presents the three-dimensional models of the sensor with different b values while keeping other parameters fixed ($d_1 = 5$ μm, $d_2 = 2.4$ μm, $L = 17$ μm, $a = \sqrt{3} \times b$, $h = 40$ nm). The loss spectra of the sensor's y-pol core mode are shown in Fig. 7(b).

Under the environmental conditions of $T = 29.5°C$ and $H = 37$ Oe, the loss spectra exhibit a redshift phenomenon as b increases. This is because the increase in d_2 reduces the effective refractive index n_{eff} of the y-pol core mode. According to the formulas $n = c/v$ and $\lambda = v/f$, since the optical frequency remains constant, the wavelength λ increases, thereby causing the redshift. This is because as b increases, the average refractive

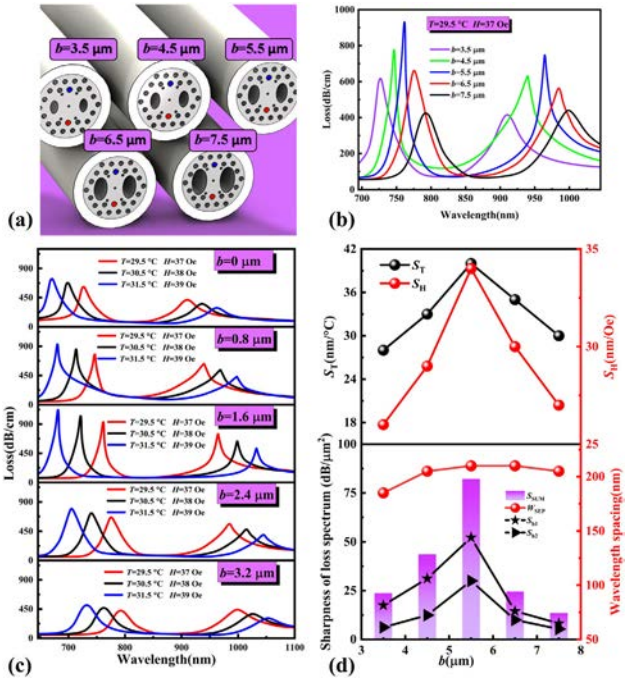

Fig. 7. When b varies between 3.5 and 7.5 μm, (a) 3D models of the sensor, (b) changes in the loss spectrum under fixed T and H conditions, (c) comparison of the sensor's loss spectra under different T and H conditions, and (d) summary and comparison of the sensor performance as a function of b.

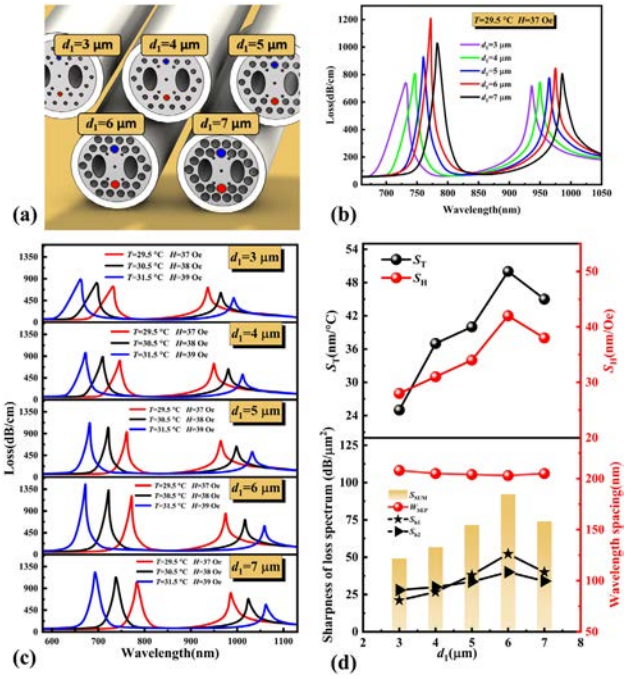

Fig. 8. When d_1 varies between 3 and 7 μm, (a) 3D models of the sensor, (b) changes in the loss spectrum under fixed T and H conditions, (c) comparison of the sensor's loss spectra under different T and H conditions, and (d) summary and comparison of the sensor performance as a function of d_1.

index in the central region of the sensor decreases, leading to a reduction in the n_{eff} of the y-pol core mode and thus producing a redshift. Figure 7(c) shows the loss spectra when multiple sets of magnetic fields and temperatures change simultaneously. Figure 7(d) summarizes the performance characteristics of the sensor. As shown, when $b = 5.5$ μm, the S_H and S_T of the sensor reach their maximum values, and the total sharpness S_{SUM} also reaches its maximum value, which are 34.564 nm/Oe, 40°C/nm, and 79.42 dB/μm^2, respectively. Compared with the optimization results of the previous step, after this optimization, the detection performance of the sensor is overall improved. Similarly, the W_{SEP} shows no significant change with the increase of b. Considering all factors, $b = 5.5$ μm is ultimately selected.

C. Cladding Air Hole Diameter

After determining $d_2 = 2.4$ μm and $b = 5.5$ μm, we optimized the cladding air hole diameter d_1, and the results are shown in Figs. 8(a)–8(d). The optimization range of d_1 was set between 3 and 7 μm. The reason is that when d_1 is less than 3 μm, the air holes in the cladding cannot effectively confine the light beam in the core region, leading to a weakening or even disappearance of the SPR effect. When d_1 is greater than 7 μm, the spacing between air holes is too narrow, prone to deformation or even rupture during the fiber drawing process. Figure 8(a) presents the three-dimensional models of the sensor with different d_1 values while other parameters are fixed ($d_2 = 2.4$ μm, $b = 5.5$ μm, $L = 17$ μm, $a = \sqrt{3} \times b$, $h = 40$ nm). The loss spectra of the sensor's y- pol core mode are shown in Fig. 8(b). Under the environmental conditions of $T = 29.5$°C and $H = 37$ Oe, as d_1 increases, the loss spectra exhibit a blue shift phenomenon. This is because when d_1 increases, the proportion of air holes in the cladding increases, thus leading to an increase in the relative refractive index of the core. According to the formulas $n = c/v$ and $\lambda = v/f$, since the frequency of light remains constant in different media, the wavelength λ decreases, thereby causing the blue shift. Figure 8(c) shows the loss spectra when multiple sets of H and T change simultaneously. Figure 8(d) summarizes the performance characteristics of the sensor. As shown, when $d_1 = 5$ μm, the S_H and S_T of the sensor reach their maximum values, and the total sharpness S_{SUM} also reaches its maximum value, which are 42.628 nm/Oe, 50.034°C/nm, and 92.82 dB/μm^2, respectively. Compared with the optimization results of the previous step, the sensor's performance is further improved. The W_{SEP} remains almost unchanged with the increase of b. Considering all factors, $d_1 = 5$ μm is ultimately selected.

D. Gold Film Thickness

Finally, after determining $d_2 = 2.4$, $b = 5.5$, and $d_1 = 5$ μm, we optimized the gold film thickness h, and the results are shown in Figs. 9(a)–9(d). The optimization range of h was set between 30 and 50 nm. The reason is that when $h < 30$ nm, the sensor exhibits excessively high loss, and the light transmittance is too low. When $h > 50$ nm, the SPR effect for this structural parameter begins to disappear, and there is no distinct loss peak. Figure 9(a) presents the three-dimensional models of the sensor with different h values while other parameters are fixed ($d_1 = 5$ μm, $d_2 = 2.4$ μm, $b = 5.5$ μm, $L = 17$ μm, $a = \sqrt{3} \times b$). The loss spectra of the sensor's y-pol core mode

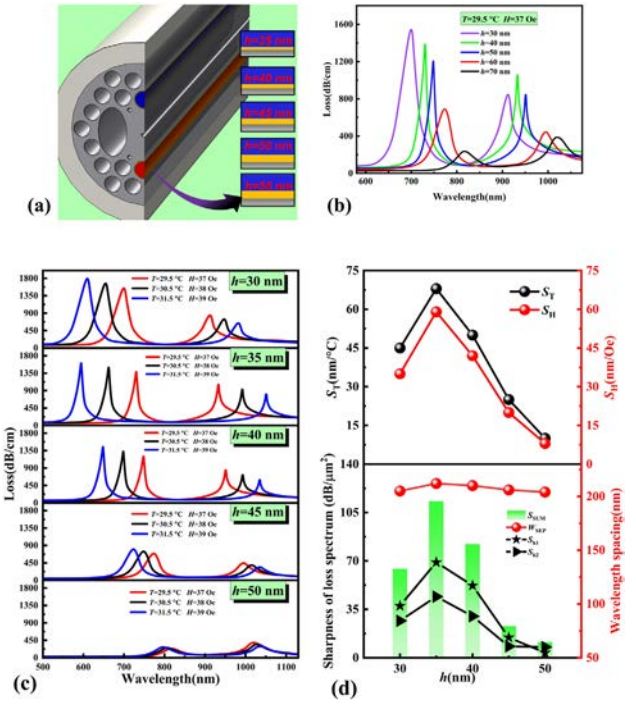

Fig. 9. When h varies between 30 and 50 nm, (a) 3D models of the sensor, (b) changes in the loss spectrum under fixed T and H conditions, (c) comparison of the sensor's loss spectra under different T and H conditions, and (d) summary and comparison of the sensor performance as a function of h.

are shown in Fig. 9(b). Under the environmental conditions of $T = 29.5°C$ and $H = 37$ Oe, as h increases, the loss spectra exhibit a redshift phenomenon. This is because when the wavelength is between 500 and 1200 nm, the refractive index of gold is approximately 0.5 RIU, which is much lower than that of air and optical fiber. Increasing h reduces the refractive index near the gold film, leading to a decrease in the n_{eff} of the SPP mode in the gold film, and the n_{eff} of the y-pol core mode phase-matched with it also decreases. Since the frequency of light remains constant when propagating in different media, according to the formulas $n = c/v$ and $c = v/f$, as h increases, the wavelength λ increases, resulting in a redshift phenomenon. Figure 9(c) shows the loss spectra when multiple sets of H and T change simultaneously. Figure 9(d) summarizes the performance characteristics of the sensor. As shown in the figure, when $h = 35$ nm, the S_H and S_T of the sensor reach their maximum values, and the total sharpness S_{SUM} also reaches its maximum value, which are 45.463 nm/Oe, 64.716°C/nm, and 113.27 dB/μm^2, respectively. Compared with the previous optimization results, the sensor's sensitivity and other performances are significantly improved, while the resonance peak spacing remains almost unchanged with the increase of h. Considering all factors, $h = 35$ nm is ultimately selected.

5. SENSING CHARACTERISTICS

The sensor can achieve simultaneous detection of magnetic field and temperature according to the experimental setup in Fig. 10. Single-mode fibers (SMF) are used for optical signal transmission. Specific environmental conditions are simulated

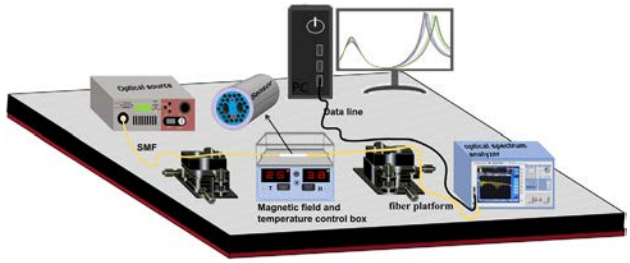

Fig. 10. Schematic diagram of the setup for magnetic field and temperature detection.

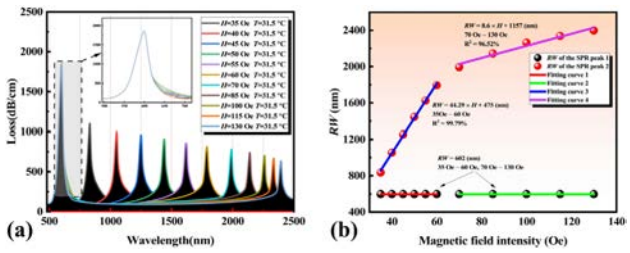

Fig. 11. (a) Loss spectra for different H between 35 Oe and 130 Oe and (b) fitted results of the RW shift with H.

by a magnetic field and a temperature control box. A broadband light source is employed to provide optical signals in the 500–2500 nm wavelength band. An optical spectrum analyzer (OSA) converts optical signals into electrical signals and modulates them. The modulated electrical signal data are analyzed by a PC [35].

Figure 11 shows the magnetic field sensing characteristics of the optimized sensor. As shown in Fig. 11(a), when $T = 31.5°C$ and H varies between 35 Oe and 130 Oe, SPR peak 1 does not shift. The linear fitting between RW and H is shown in Fig. 11(b). The fitting curve for SPR peak 1 is a horizontal line (RW = 60 nm), indicating that the temperature detection crosstalk caused by magnetic field changes is zero. Since the relationship between RW and H is nonlinear, fitting curves for different H ranges are plotted. For SPR peak 2, when H is between 35 Oe and 60 Oe, $\text{RW} = 44.29\,H + 475$ (nm) with a coefficient of determination (R^2) of 99.79%. Between 80 Oe and 130 Oe, $\text{RW} = 8.6\,H + 1157$ (nm) with $R^2 = 96.52\%$. As can be seen from Eq. (4), when H is around 30 Oe, the rate of change of the refractive index of the magnetic fluid with respect to H is the largest. Therefore, in the vicinity of $H > 30$ Oe, the S_H reaches its maximum. This conclusion can be verified from Fig. 11(b): as H increases, the slope of the fitting line decreases. The S_H of this sensor can reach 67.35 nm/Oe near $H = 31$ Oe.

Figure 12 shows the temperature sensing characteristics of the optimized sensor. PDMS behaves as a viscous liquid at high temperatures or high flow rates and as an elastic solid at low temperatures or low flow rates [36]. Therefore, both excessively high and low T can impair the linear stability of the sensor. Figure 12(a) shows the y-pol core mode loss spectra when $H = 39.5$ Oe and T ranges from 26.5°C to 30.5°C. SPR peak 2 does not shift. The linear fitting between RW and T is shown in Fig. 11(b). The fitting curve for SPR peak 2 is a horizontal line (RW = 1023 nm), indicating that the magnetic field detection crosstalk caused by T changes is zero. The linear

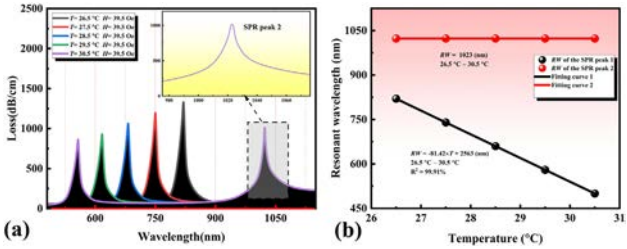

Fig. 12. (a) Loss spectra for T between 26.5°C and 30.5°C and (b) fitted results of the RW shift with T.

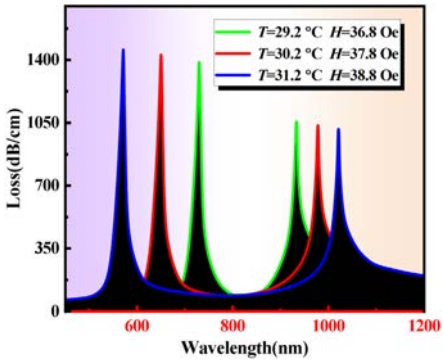

Fig. 13. Loss spectrum when the H and T alter simultaneously.

fitting curve for SPR peak 1 is RW $= -81.42\ T + 2563$ (nm) with $R^2 = 99.91\%$. From the linear fitting curve, it can be seen that the relationship between RW and T is linear. Within the range of 26.5°C to 30.5°C, the average temperature sensitivity of this sensor can reach 81.42 nm/°C.

As shown in Fig. 13, we analyzed the y-pol core mode loss spectra of the PM-PCF dual-parameter sensor when T and H simultaneously increase within the ranges of 29.2–31.2°C and 36.8–38.8 Oe, respectively. It is evident that SPR peak 1 exhibits a blue shift, while SPR peak 2 exhibits a red shift. As previously mentioned, this PM-PCF dual-parameter magnetic field and temperature sensor achieves zero-crosstalk detection based on the loss spectra. By separately calculating the shifts of the two loss peaks, both the H and T can be accurately detected.

To demonstrate the advantages of this sensor, Table 1 compares the properties of different magnetic field and temperature dual-parameter sensors. Our PM-PCF dual-parameter sensor has achieved zero-crosstalk detection for the first time. Compared with the highest sensitivity reported so far, our design nearly doubles it.

6. CONCLUSION

A PM-PCF-based dual-parameter magnetic field and temperature sensor is proposed and analyzed. This sensor is a polarization-maintaining high-loss sensor designed based on a light-guiding photonic crystal fiber structure. A rectangular core structure is formed by two large elliptical holes. Thanks to the high refractive index difference between air and glass, the optical field can be confined to a very small core region, which gives the sensor excellent confinement and greatly enhances the coupling effect of the SPR phenomenon. The loss spectrum of the dual-parameter sensor based on this dimensional structure exhibits high-loss peaks, eliminating the crosstalk problem when simultaneously detecting magnetic fields and temperatures. Magnetic fields and temperatures can be accurately detected by separately calculating the shifts of the two loss peaks. At the same time, five circular air holes are arranged in the core to fine-tune the SPR coupling process, achieving ultra-high sensitivity. The structural parameters of the sensor are optimized mainly based on the sensor sensitivity and the sharpness of the loss peaks. Finally, the parameters are determined as follows: $d_1 = 5\ \mu m$, $d_2 = 2.4\ \mu m$, $b = 5.5\ \mu m$, $L = 17\ \mu m$, $a = \sqrt{3} \times b$, $h = 35$ nm. We analyzed the sensitivity of the sensor when T and H vary within the ranges of 26.5–30.5°C and 30–130 Oe, respectively. The numerical results show that the maximum magnetic field sensitivity can reach 67.35 nm/Oe, and the average temperature sensitivity can reach 81.42 nm/°C.

Table 1. Comparison of Different Dual-Parameter Sensors for Magnetic Field and Temperature Sensing

References	Fiber	Crosstalk	Max Magnetic Sensitivity	Max Temperature Sensitivity	Cross Section
[10]	MMF	Yes	0.012 nm/Oe	1.662 nm/°C	
[13]	ACF	Yes	0.3 nm/Oe	−10.8 nm/°C	
[37]	PCF	Yes	0.235 nm/Oe	1.104 nm/°C	
[38]	PCF	Yes	0.312 nm/Oe	1.993 nm/°C	
[14]	DHF	Yes	6.4 nm/Oe	44.6 nm/°C	
[15]	CF	Yes	20.207 nm/Oe	8.423 nm/°C	
This Work	PCF	No	67.35 nm/Oe	81.42 nm/°C	

This represents nearly a twofold improvement over the current state of the art. In addition, the longstanding crosstalk problem in dual-parameter temperature and magnetic field fiber sensors has been overcome. At a precision level of 0.001 nm, the shift of the loss peak caused by crosstalk is zero, achieving zero-crosstalk detection.

Funding. National Natural Science Foundation of China (12304480, 62305223); Natural Science Foundation of Heilongjiang Province (JQ2023F001); Local Universities Reformation and Development Personnel Training Supporting Project from Central Authorities, Natural Science Foundation of Heilongjiang Province (LH2021F007); China Postdoctoral Science Foundation (2020M670881); Natural Science Foundation of Guangdong Province (2022A1515110971); Fundamental Project Natural Science Foundation of Heilongjiang Province (LH2022F004); City University of Hong Kong Donation Research Grants (DON-RMG 9229021, 9220061).

Acknowledgment. This work was jointly supported by the National Natural Science Foundation of China [12304480], Heilongjiang Provincial Natural Science Foundation of China [JQ2023F001], Local Universities Reformation and Development Personnel Training Supporting Project from Central Authorities, Natural Science Foundation of Heilongjiang Province [LH2021F007], China Postdoctoral Science Foundation funded project [2020M670881], the National Natural Science Foundation of China (62305223), and Natural Science Foundation of Guangdong Province (2022A1515110971); the project was supported in part by the Fundamental Project Natural Science Foundation of Heilongjiang Province (LH2022F004), as well as City University of Hong Kong Donation Research Grants [DON-RMG 9229021 and 9220061].

Disclosures. The authors declare no conflicts of interest.

Data availability. Data underlying the results presented in this paper are not publicly available at this time but may be obtained from the authors upon reasonable request.

REFERENCES

1. H. Zhang, X. Li, X. Zhou, *et al.*, "Label-free ultrasensitive cholesterol detection based on SPR optical fiber sensor," IEEE Sens. J. **24**, 40972–40978 (2024).
2. X. Manyosa, D. Roma-Dollase, M. Arqué, *et al.*, "MEMS miniaturized low-noise magnetic field sensor for the observation of sub-millihertz magnetic fluctuations in space exploration," Measurement **230**, 114489 (2024).
3. J. P. Gill and B. K. Taylor, "Navigation by magnetic signatures in a realistic model of Earth's magnetic field," Bioinspir. Biomim. **19**, 036006 (2024).
4. R. Yang, H. Wang, W. Luo, *et al.*, "Cumulative error calibration of fluxgate sensor considering temperature effects," IEEE Trans. Instrum. Meas. **73**, 9517408 (2024).
5. H. Okeil and G. Wachutka, "4H-SiC lateral magnetotransistor with sub-microtesla in-plane magnetic field detectivity," IEEE Electron. Device Lett. **45**, 2173–2176 (2024).
6. U. I. Cicek, D. J. Southee, and A. A. Johnson, "The development and characterisation of 3D-printed multi-material thermistor," Addit. Manuf. **94**, 104510 (2024).
7. D. M. Kim, H. J. Kwak, D. Y. Shin, *et al.*, "Optimal fabrication of a thin-film thermocouple (TFTC) using Alumel/chromel junctions," Heliyon **10**, e26128 (2024).
8. A. Hassani and M. Skorobogatiy, "Design criteria for microstructured-optical-fiber-based surface-plasmon-resonance sensors," Opt. Soc. Am. B **24**, 1423–1429 (2007).
9. H. Liu, C. Tan, C. Zhu, *et al.*, "Simultaneous measurement of temperature and magnetic field based on directional resonance coupling in photonics crystal fibers," Opt. Commun. **391**, 111–115 (2017).
10. J. Fu, S. Pu, Z. Hao, *et al.*, "Reflective magnetic field and temperature dual-parameter sensor based on no-core fiber probe," Opt. Laser Technol. **174**, 110550 (2024).
11. H. Liu, C. Chen, H. Wang, *et al.*, "Simultaneous measurement of magnetic field and temperature based on surface plasmon resonance in twin-core photonics crystal fiber," Optik **203**, 164007 (2020).
12. D. Wang, Z. Yi, G. Ma, *et al.*, "Two-channel photonics crystal fiber based on surface plasmon resonance for magnetic field and temperature dual-parameter sensing," Phys. Chem. Chem. Phys. **24**, 21233–21241 (2022).
13. M. Liu, X. Leng, W. Ni, *et al.*, "Simultaneous and ultrasensitive measurement of refractive index and temperature based on SPR of hollow-core anti-resonant fibers," Plasmonics **19**, 3091–3100 (2024).
14. H. Fu, Z. Sheng, W. Gao, *et al.*, "Ultra-high sensitive dual-parameter sensor based on double-hole fiber for simultaneous detection of magnetic field and temperature," Opt. Express **32**, 20175–20193 (2024).
15. C. Liu, W. Wang, J. Lv, *et al.*, "Coreless optical fiber sensor based on surface plasmon resonance for simultaneous measurement of magnetic field and temperature," IEEE Sens. J. **25**, 21581–21588 (2025).
16. J. Wang, L. Pei, J. Wang, *et al.*, "A high sensitivity dual-parameter sensor based on glycerin filled fine-core polarization maintaining photonics crystal fiber," Opt. Fiber Technol. **55**, 102139 (2020).
17. C. Liu, J. Wang, J. Lv, *et al.*, "Economical and easily implemented Vernier effect bubble microcavity FPI for strain sensing with extreme low-temperature cross-sensitivity," Infrared Phys. Technol. **150**, 105939 (2025).
18. H. Xiao, H. Li, B. Wu, *et al.*, "Elliptical hollow-core optical fibers for polarization-maintaining few-mode guidance," Opt. Fiber Technol. **48**, 7–11 (2019).
19. Y. Liu, H. Chen, Q. Chen, *et al.*, "Experimental study on dual-parameter sensing based on cascaded Sagnac interferometers with two PANDA fibers," J. Lightw. Technol. **40**, 3090–3097 (2022).
20. A. L. Tomashuk, P. F. Kashaykin, S. L. Semjonov, *et al.*, "Comparison study of radiation-resistant polarization-maintaining PANDA fibers with undoped-and N-doped-silica core," J. Lightw. Technol. **38**, 5817–5824 (2020).
21. R. Ahmad, M. F. Yan, J. W. Nicholson, *et al.*, "Polarization-maintaining, large-effective-area, higher-order-mode fiber," Opt. Lett. **42**, 2591–2594 (2017).
22. H. Xiao, H. Li, and S. Jian, "Hole-assisted polarization-maintaining few-mode fiber," Opt. Laser Technol. **107**, 162–168 (2018).
23. Z. Cai, B. Li, Z. Bai, *et al.*, "Encrypted optical fiber tag based on encoded fiber Bragg grating array," Int. J. Extreme Manuf. **5**, 035502 (2023).
24. M. Zou, C. Liao, Y. Chen, *et al.*, "3D printed fiber-optic nanomechanical bioprobe," Int. J. Extreme Manuf. **5**, 015005 (2023).
25. D. Zhu, S. Jiang, Y. Wang, *et al.*, "Three-dimensional direct lithography of stable quantum dots in hybrid glass," Int. J. Extreme Manuf. **7**, 035503 (2025).
26. D. Y. Shin, C. Kim, Y. J. Moon, *et al.*, "Ultrasonic punching with inkjet-printed dot array for fabrication of perforated metal pattern as transparent heater," Adv. Eng. Mater. **26**, 2400377 (2024).
27. J. S. Velázquez-González, D. Monzón-Hernández, F. Martínez-Piñón, *et al.*, "Surface plasmon resonance-based optical fiber embedded in PDMS for temperature sensing," IEEE J. Sel. Top. Quantum Electron. **23**, 126–131 (2017).
28. H. Gao, H. Hu, Y. Zhao, *et al.*, "Highly-sensitive optical fiber temperature sensors based on PDMS/silica hybrid fiber structures," Sens. Actuators A Phys. **284**, 22–27 (2018).
29. W. Liu, H. He, Y. You, *et al.*, "Compact SPR magnetic field sensor based on an inner wall waveguide fiber filled with magnetic fluid," Opt. Lett. **50**, 1488–1491 (2025).
30. J. Wang, X. Lu, C. Mi, *et al.*, "Ultra-high sensitivity photonics crystal fiber sensor based on dispersion turning point sensitization of surface plasmonic polariton modes for low RI liquid detection," Opt. Express **32**, 32895–32908 (2024).
31. Q. Feng, L. He, L. Wu, *et al.*, "High energy-dissipation PDMS polymer-fluid-gels over an ultra-wide temperature range," Chem. Eng. J. **491**, 152108 (2024).
32. L. Sun, S. Gao, B. Xu, *et al.*, "Dual-tapered fiber Mach–Zehnder interferometric magnetic field sensor based on magnetic fluid," Electr. Eng. **107**, 6891–6900 (2024).

33. Z. Yin and X. Jing, "Low crosstalk dual-parameter no-core fiber based SPR sensor with differentiated silver film thickness," IEEE Sens. J. **24**, 22404–22409 (2024).
34. M. R. Khodatars Dashtmian, V. Fallahi, S. Olyaee, *et al.*, "Highly sensitive dual-side polished SPR PCF sensor for ultra-wide analyte range in the visible to near-IR operating band," Opt. Quantum Electron. **56**, 1187 (2024).
35. H. Li, R. Fu, X. Yan, *et al.*, "Dual-channel high sensitivity temperature and magnetic field sensor based on Mach–Zehnder interference and surface plasmon resonance," IEEE Sens. J. **24**, 36768–36775 (2024).
36. V. Genovés, L. Maini, C. Roman, *et al.*, "Variation in the viscoelastic properties of polydimethylsiloxane (PDMS) with the temperature at ultrasonic frequencies," Polym. Test. **124**, 108067 (2023).
37. J. Liu, J. Dong, S. Hou, *et al.*, "Design of a gold-nanowires embedded PCF for magnetic field and temperature sensing," Plasmonics **20**, 2457–2466 (2024).
38. G. Wang, H. Huang, J. Sun, *et al.*, "Temperature and magnetic field fiber sensor with high sensitivity and linearity based on surface plasmon resonance," Opt. Commun. **574**, 131140 (2025).